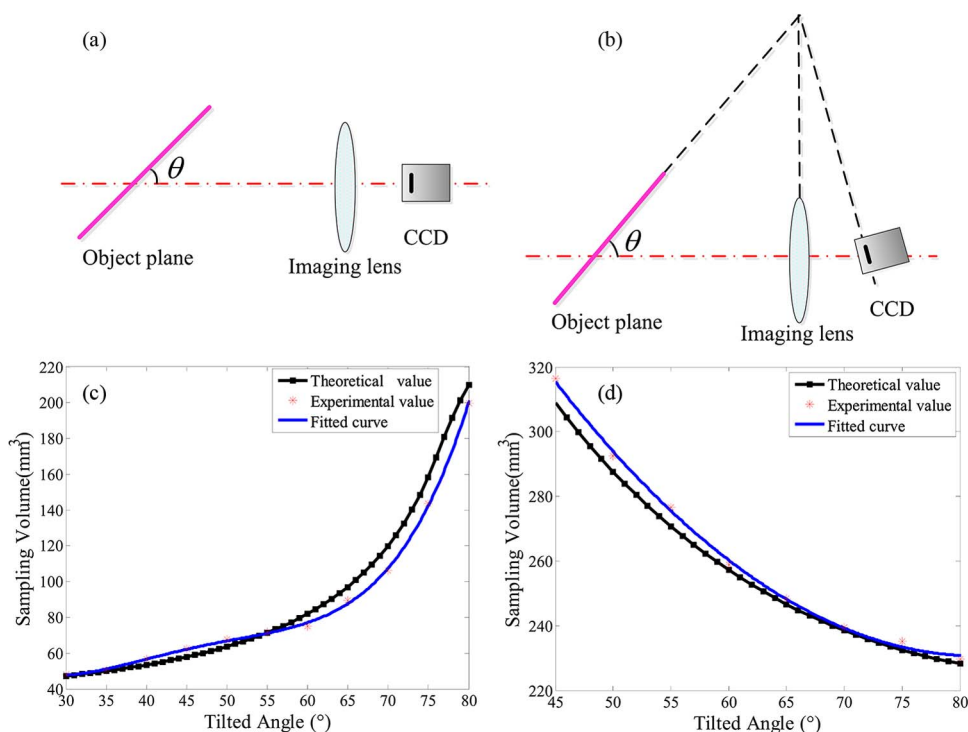


Theoretical Analysis and Experimental Validation of Sampling Volume in Tilted Imaging System

Volume 7, Number 6, December 2015

Hongxia Zhang
Jing Liu
Mengran Zhai
Ye Zhou
Dagong Jia
Tiegen Liu



DOI: 10.1109/JPHOT.2015.2495126
1943-0655 © 2015 IEEE

Theoretical Analysis and Experimental Validation of Sampling Volume in Tilted Imaging System

Hongxia Zhang, Jing Liu, Mengran Zhai, Ye Zhou,
Dagong Jia, and Tiegeng Liu

¹College of Precision Instrument and Optoelectronics Engineering,
Tianjin University, Tianjin 300072, China

²Key Laboratory of Optoelectronics Information Technical Science,
Education Ministry of China (EMC), Tianjin 300072, China

DOI: 10.1109/JPHOT.2015.2495126

1943-0655 © 2015 IEEE. Translations and content mining are permitted for academic research only.

Personal use is also permitted, but republication/redistribution requires IEEE permission.

See http://www.ieee.org/publications_standards/publications/rights/index.html for more information.

Manuscript received September 2, 2015; revised October 19, 2015; accepted October 21, 2015.
Date of publication October 26, 2015; date of current version November 13, 2015. This work was supported by the National Natural Sciences Foundation under Grant 41275146. Corresponding author: H. Zhang (e-mail: hxzhang@tju.edu.cn).

Abstract: A method for accurately calculating the sampling volume in a tilted imaging system is proposed. Two types of tilted imaging systems are investigated, i.e., Type I (only the object plane is inclined to the optical axis) and Type II (both the object plane and the image plane are inclined to the optical axis). Based on geometrical optics, the sampling volumes of these two types of tilted imaging systems have been simulated. Compared with the central magnification of an imaging system and the focal length and F -number of the imaging lens, the effect of the tilted angle of the object plane on the sampling volume is determined to be more important. A tilted imaging experimental setup has been established, calibration plate images at various tilted angles and positions have been acquired, and the sampling volume has been obtained by image processing. The experimental results are in very good agreement with the theoretical predictions. As the tilted angle increases, for the Type-I system, the sampling volume increases, whereas for the Type-II system, the sampling volume decreases. In addition, the sampling volume of the Type-II system is larger than that of the Type-I system. Knowledge of the sampling volume is necessary in many quantitative applications of tilted imaging systems.

Index Terms: Tilted imaging system, sampling volume, Scheimpflug principle, tilted angle.

1. Introduction

An optical imaging system has important applications in many fields because it provides a lot of information about an object plane. A conventional imaging system satisfies the condition that the object plane, lens plane, and image plane are parallel to each other. However, this type of imaging system has been unable to meet the requirements of some special fields; thus, the tilted imaging system has attracted much attention. There are two types of tilted imaging systems: Type-I (only the object plane is inclined to optical axis) and Type-II (both the object plane and image plane are inclined to the optical axis). Type-I systems are widely used in the glare point imaging technique. Glare point imaging described by van de Hulst and Wang [1] is a relatively new type of particle size measurement technique and has important applications in spray flows. Recently, scholars have performed extensive research on droplet size and

velocity measurements in glare point imaging systems [2]–[4]. Moreover, a combination of in-focus and out-of-focus imaging has been simultaneously used to determine the size and velocity of droplets [5]–[7]. Type-II systems follow the Scheimpflug principle, which has important applications in ophthalmology and laser triangulation. These systems have been applied to assess the anterior chamber configuration [8]–[11]. The anterior chamber depth has been measured by Kashiwagi *et al.* [12]. Grewal has discussed the clinical applications and limitations of Scheimpflug imaging in modern cataract surgery patients [13] and Masters has studied the 3-D microscopic tomographic imaging of the cataract in a human lens in vivo [14]. Based on the Scheimpflug principle, the design and manufacture of a multi-detector triangulation laser probe has been presented by Shiou and Cheng [15] and a novel structure of 3-D camera based on laser double triangulation displacement sensor is proposed by Wang *et al.* [16]. Analysis of imaging for laser triangulation sensors under Scheimpflug principle has been proposed by Miks *et al.* [17]. Type-II systems can also be used for particle image velocimetry in liquid flows [18], [19]. A model to recover distorted particle image velocimetry images of a droplet has been developed for an accurate flow field by He and Duan [20]. In addition, newly developed fringe projection 3-D microscopy is presented by Yin *et al.* and the Scheimpflug principle is employed in system to make full use of the limited depth of field [21].

The sampling volume of an imaging system is the volume in the object space that can produce clear images on the focused image plane. It is the intersection between the illumination beam, imaging range of the object space limited by the size of the charge-coupled device (CCD) target surface, and plane between the front and back depth of field. Therefore, the sampling volume is correlated to the tilted angle, focal length, F -number, central magnification, size of the CCD target surface, and thickness of the illumination beam. The object plane of a conventional imaging system is rectangular due to the size limitation produced by the CCD target surface, whereas the object plane of a tilted imaging system is trapezoidal because different positions on the object plane have different magnifications. Therefore, the sampling volume of a tilted imaging system is complicated. Knowledge of the sampling volume is necessary in many quantitative applications of tilted imaging systems. Up until now, a measurement method for the sampling volume of a tilted imaging system has not yet been proposed.

Therefore, the objective of this study is to accurately calculate the sampling volume of these two types of tilted imaging systems. Based on geometrical optics, the formula for the sampling volume has been derived, and the effects of the tilted angle, central magnification, focal length, and F -number on the sampling volume have been analyzed. A tilted imaging experimental setup has been established, and through both theoretical and experimental analyses, the sampling volume of the tilted imaging system has been calculated.

2. Theoretical Model

Diagrams of the two types of tilted imaging systems are presented in Fig. 1. Fig. 1(a) is a Type-I system; the CCD target surface is parallel to the lens plane, and the object plane tilts toward the optical axis with a tilted angle θ . Fig. 1(b) is a Type-II system, which follows the Scheimpflug principle. The Scheimpflug principle states that the CCD image plane, lens plane, and object plane intersect at a line and that the object plane tilts toward the optical axis with a tilted angle θ . In the following sections, we use OP to denote the object plane, LP to denote the lens plane, and IP to denote the image plane.

2.1. Model of Type-I System

LP and IP are parallel, and OP tilts toward the optical axis with a tilted angle θ , as illustrated in Fig. 2. Assuming that points M and N are on the edge of the plane of focus (PoF), when the lens is in focus on point N , its image N' is on IP. The images of Q_2 and Q_4 are Q_2' and Q_4' , after and before IP, respectively, whose images are circles of confusion with a diameter of δ on IP. Due to the size limitation of the CCD target surface, the imaging range of the object space is restricted; hence, the quadrilateral area in the paper surface surrounded by four points

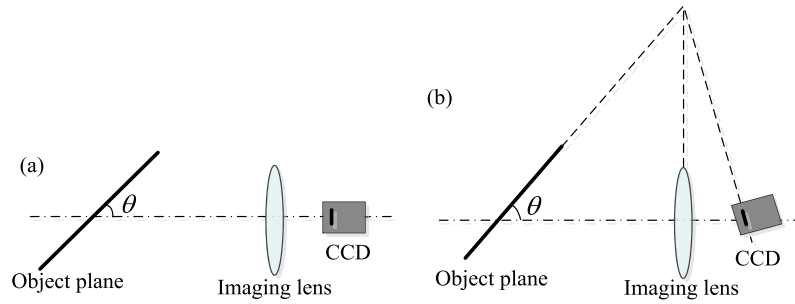


Fig. 1. Diagrams of tilted imaging systems. (a) Type-I and (b) Type-II.

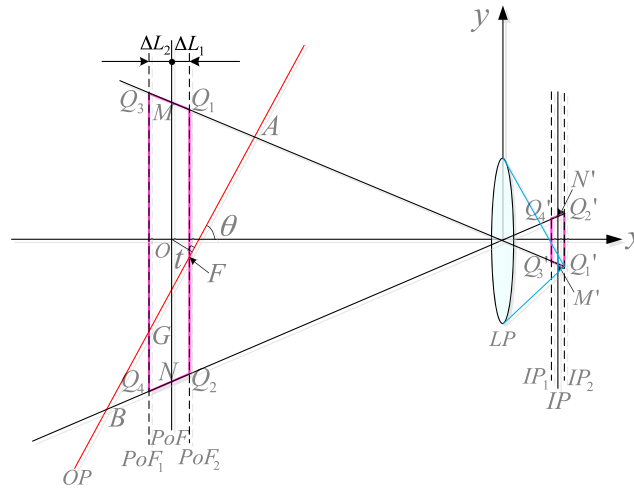


Fig. 2. Theoretical model of a Type-I system.

$Q_1, Q_2, Q_3,$ and Q_4 is the region of the depth of field. Assuming points $A, B, F,$ and G are on the central horizontal line of OP , as illustrated in Fig. 3, points A and B are on the edge of OP , points F and G are on the edge of depth of field, and $h_A, h_B, h_F,$ and h_G are the lengths of the trapezoidal bottom side through the corresponding point on OP , respectively. The coordinate system is defined in Fig. 2, and t , which is the parallel displacement distance of OP , is positive when it is close to LP and negative when it is away from LP . Assuming that u_* denotes the object distance of its subscript and v_* denotes the image distance of its subscript, u_* and v_* are unsigned numbers. For example, the object distance of the central point O is u_o , its image distance is v_o , and its magnification is β_o .

According to the similarity of triangles and Gaussian equation, the depth of field of this imaging system is

$$\begin{aligned} \text{front depth of field : } \Delta L_1 &= u_o - f \cdot d_a \cdot v_o / (d_a - \delta) / [d_a \cdot v_o / (d_a - \delta) - f], \\ \text{back depth of field : } \Delta L_2 &= f \cdot d_a \cdot v_o / (\delta + d_a) / [d_a \cdot v_o / (\delta + d_a) - f] - u_o, \\ \text{depth of field : } &f \cdot d_a \cdot v_o / (\delta + d_a) / [d_a \cdot v_o / (\delta + d_a) - f] - f \cdot d_a \cdot v_o / (d_a - \delta) / [d_a \cdot v_o / (d_a - \delta) - f], \end{aligned} \quad (1)$$

where f is the focal length of the imaging lens, and d_a is the clear aperture of the imaging lens.

The equations of u_A and u_B in terms of the similarity of triangles are

$$u_A = (u_o - t / \sin \theta) \cdot \tan \theta / [\tan \theta + a / (2v_o)], \quad (2)$$

$$u_B = (t / \sin \theta - u_o) \cdot \tan \theta / [a / (2v_o) - \tan \theta], \quad (3)$$

where a is the width of the CCD target surface.

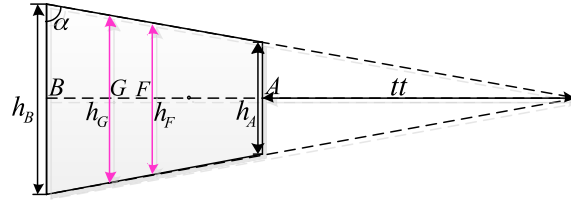


Fig. 3. Trapezoidal OP.

The equations for h_A and h_B are

$$h_A = b \cdot u_A / v_o, \quad (4)$$

$$h_B = b \cdot u_B / v_o, \quad (5)$$

where b is the height of the CCD target surface.

The distance between point A and point B , which is the height of the trapezoidal OP, is

$$\overline{AB} = (u_B - u_A) / \cos \theta. \quad (6)$$

The base angle of trapezoidal OP is

$$\tan \alpha = 2\overline{AB} / (h_B - h_A). \quad (7)$$

The equations for u_F and u_G are

$$u_F = u_o - \Delta L_1, \quad (8)$$

$$u_G = u_o + \Delta L_2. \quad (9)$$

tt , as shown in Fig. 3, is expressed as

$$tt = h_B / 2 \cdot \tan \alpha - (u_B - u_A) / \cos \theta. \quad (10)$$

The distances of the line segments \overline{BF} , \overline{AG} , \overline{AF} , \overline{FG} are

$$\overline{BF} = (u_B - u_F) / \cos \theta, \quad (11)$$

$$\overline{AG} = (u_G - u_A) / \cos \theta, \quad (12)$$

$$\overline{AF} = (u_o - u_A - \Delta L_1) / \cos \theta, \quad (13)$$

$$\overline{FG} = \Delta L / \cos \theta. \quad (14)$$

The equations for h_F and h_G are

$$h_F = h_A \cdot (tt + \overline{AF}) / tt, \quad (15)$$

$$h_G = h_A \cdot (tt + \overline{AF} + \Delta L / \cos \theta) / tt. \quad (16)$$

According to (1)–(16), the clear area that is trapezoidal on OP is

$$C.S = \begin{cases} (h_F + h_G) \cdot \overline{FG} / 2, & u_G \leq u_B, u_F \geq u_A \\ (h_A + h_B) \cdot \overline{AB} / 2, & u_G > u_B, u_F < u_A \\ (h_A + h_G) \cdot \overline{AG} / 2, & u_G \leq u_B, u_F \leq u_A \\ (h_F + h_B) \cdot \overline{BF} / 2, & u_G > u_B, u_F > u_A \\ 0, & u_G < u_A \text{ or } u_B < u_F. \end{cases} \quad (17)$$

Therefore, the sampling volume is each clear area of OP to the integral of the displacement distance of OP

$$V = \int_{-c/2}^{c/2} C.S dt \quad (18)$$

where c is the thickness of the illumination beam.

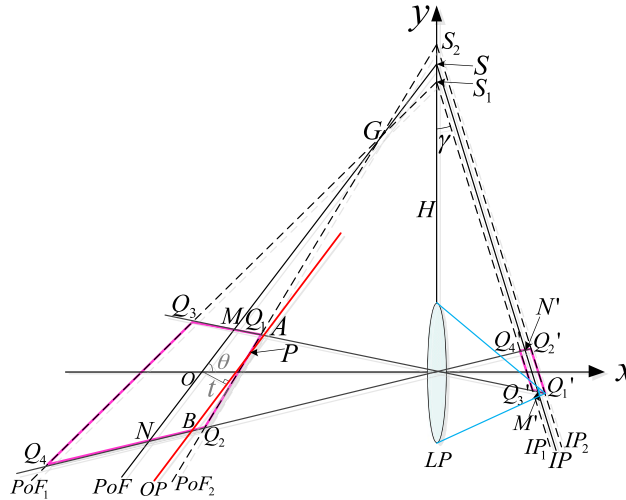


Fig. 4. Theoretical model of a Type-II system.

2.2. Model of Type-II System

The Scheimpflug principle inferred from projective geometry is a geometric rule that describes the orientation of PoF of an optical system when LP is not parallel to IP. The extension of IP and LP meet at a line, which is called the Scheimpflug line (S). PoF, which tilts toward the optical axis with a tilted angle θ , also passes through the Scheimpflug line, as illustrated in Fig. 4. Under this condition, a planar object that is not parallel to IP can be completely in focus. The focus is adjusted by rotating the PoF rather than displacing it along the optical axis. The rotation axis (G) is the intersection between the front focal plane of the lens and a plane not only through the center of the lens but also parallel to IP. As IP is moved from IP_1 to IP_2 , the PoF rotates about the axis G from position PoF_1 to position PoF_2 , and S moves from position S_1 to position S_2 [22].

When the Scheimpflug principle is employed, the depth of field becomes wedge shaped with the apex of the wedge at the rotation axis G . The quadrilateral area surrounded by four points Q_1, Q_2, Q_3, Q_4 is the depth of field because of the size limitation caused by CCD target surface.

Similar to the Type-I system, the coordinate system and parallel displacement distance of OP , t , are defined. First, the coordinates of eight points $Q_1, Q_2, Q_3, Q_4, A, B, M$, and N are solved. Points M and N are on the edge of PoF, and points A and B are on the edge of OP . It is important to note that if IP is tilted with respect to LP, the circles of confusion become ellipses. Assuming that the circles of confusion are used to substitute for ellipses of confusion, the calculation method is similar to that used for the Type-I system. Then, the equations of straight lines \overline{AB} , $\overline{Q_1Q_2}$ and $\overline{Q_3Q_4}$ would be solved. Eventually, the clear area that is trapezoidal on OP (perpendicular to the paper surface) would be solved.

Assuming that the distance between the Scheimpflug line and the optical center of the lens is H , and the angle between LP and IP is γ , which is expressed as

$$\tan \gamma = v_o / H = \beta_o / \tan \theta, \quad (19)$$

the equations of u_A and u_B in terms of the similarity of triangles are

$$u_A = (v_o + a/2 \cdot \sin \gamma) \cdot \tan \theta \cdot (u_o - t/\sin \theta) / [a/2 \cdot \cos \gamma - (v_o + a/2 \cdot \sin \gamma) \cdot \tan \theta], \quad (20)$$

$$u_B = (v_o - a/2 \cdot \sin \gamma) \cdot \tan \theta \cdot (t/\sin \theta - u_o) / [a/2 \cdot \cos \gamma - (v_o - a/2 \cdot \sin \gamma) \cdot \tan \theta]. \quad (21)$$

The height of points A and B are

$$y_A = (u_o - u_A - t/\sin \theta) \cdot \tan \theta, \quad (22)$$

$$y_B = (u_B - u_o + t/\sin \theta) \cdot \tan \theta. \quad (23)$$

When $t = 0$, u_A , and u_B become to u_M and u_N , and y_A and y_B become to y_M and y_N . The

equations of h_A and h_B are

$$h_A = b \cdot u_A / (v_o + a/2 \cdot \sin \gamma), \quad (24)$$

$$h_B = b \cdot u_B / (v_o - a/2 \cdot \sin \gamma). \quad (25)$$

The distance between points A and B is

$$\overline{AB} = (u_B - u_A) / \cos \theta. \quad (26)$$

The base angle of trapezoidal OP is

$$\tan \alpha = 2\overline{AB} / (h_B - h_A). \quad (27)$$

The image distance of point Q_1 is

$$v_{Q_1} = f/F \cdot (v_o + a/2 \cdot \sin \gamma) / (f/F - \delta). \quad (28)$$

Therefore, the object distance of point Q_1 is

$$u_{Q_1} = f \cdot v_{Q_1} / (v_{Q_1} - f). \quad (29)$$

The magnification of point Q_1 is

$$\beta_{Q_1} = v_{Q_1} / u_{Q_1}. \quad (30)$$

The height of point Q_1' is

$$y_{Q_1'} = v_{Q_1} / v_M \cdot a/2 \cdot \cos \gamma. \quad (31)$$

The height of point Q_1 is

$$y_{Q_1} = (v_{Q_1} / v_M \cdot a/2 \cdot \cos \gamma) / \beta_{Q_1}. \quad (32)$$

The coordinate of point Q_1 is $(-u_{Q_1}, y_{Q_1})$. Other point coordinates Q_2, Q_3 , and Q_4 can be obtained similarly.

The equations of straight lines, \overline{AB} , $\overline{Q_1Q_2}$, and $\overline{Q_3Q_4}$, are

$$(x + u_A) / (-u_B + u_A) = (y - y_A) / (-y_B - y_A), \quad (33)$$

$$(x + u_{Q_1}) / (-u_{Q_2} + u_{Q_1}) = (y - y_{Q_1}) / (-y_{Q_2} - y_{Q_1}), \quad (34)$$

$$(x + u_{Q_3}) / (-u_{Q_4} + u_{Q_3}) = (y - y_{Q_3}) / (-y_{Q_4} - y_{Q_3}). \quad (35)$$

The clear area of OP is solved as follows.

a) If $t \geq 0$, solve the coordinate of intersection P of line \overline{AB} and line $\overline{Q_1Q_2}$

$$C_S = \begin{cases} (h_p + h_B) \cdot \overline{BP} / 2, u_{Q_1} < u_P < u_{Q_2} \\ (h_A + h_B) \cdot \overline{AB} / 2, u_P \leq u_{Q_1} \\ 0, u_P \geq u_{Q_2}. \end{cases} \quad (36)$$

b) If $t < 0$, solve the coordinate of intersection P of line \overline{AB} and line $\overline{Q_3Q_4}$

$$C_S = \begin{cases} (h_p + h_B) \cdot \overline{BP} / 2, u_{Q_3} < u_P < u_{Q_4} \\ (h_A + h_B) \cdot \overline{AB} / 2, u_P \leq u_{Q_3} \\ 0, u_P \geq u_{Q_4}. \end{cases} \quad (37)$$

Here

$$h_p = h_B - 2\overline{BP} / \tan \alpha, \quad (38)$$

$$\overline{BP} = \sqrt{(x_B - x_P)^2 + (y_B - y_P)^2}. \quad (39)$$

Therefore, similar to the Type-I system, the sampling volume is

$$V = \int_{-c/2}^{c/2} C_S dt. \quad (40)$$

3. Simulation and Analysis

To verify the above analysis, the sampling volume with parameters of the tilted angle, focal length, central magnification, and F -number was simulated, as illustrated in Fig. 5. Assuming

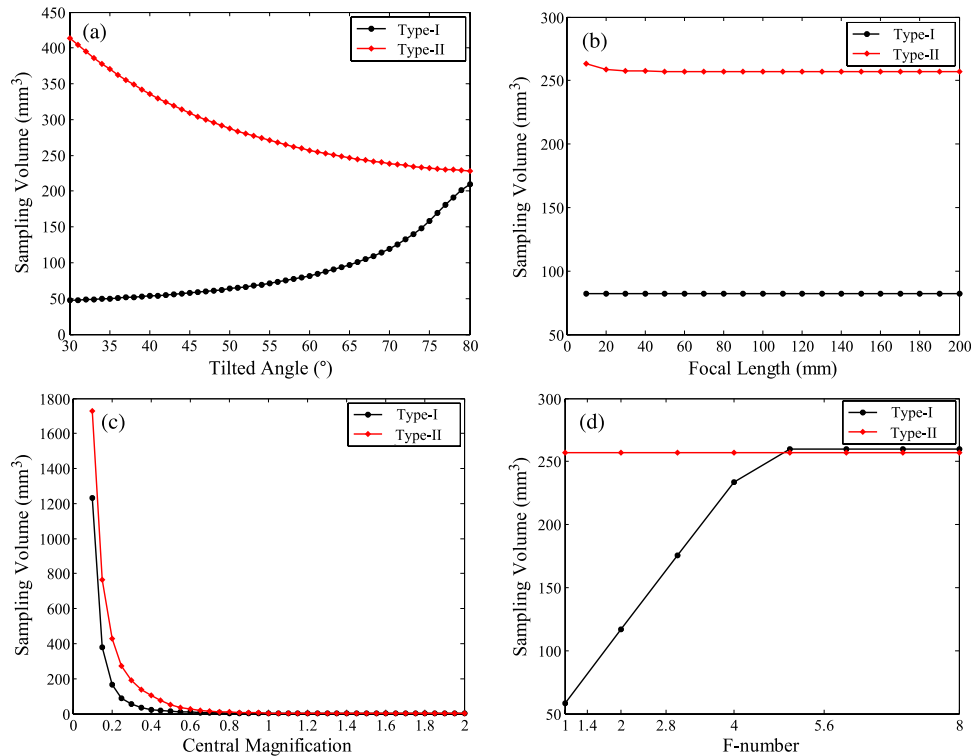


Fig. 5. Sampling volume with parameters of tilted angle, focal length, central magnification, and F -number. (a) $f = 50$ mm, $F = 1.4$, $\beta_o = 0.258$; (b) $\beta_o = 0.258$, $F = 1.4$, $\theta = 60^\circ$; (c) $f = 50$ mm, $F = 1.4$, $\theta = 60^\circ$; and (d) $\beta_o = 0.258$, $f = 50$ mm, $\theta = 60^\circ$.

that the thickness of the illumination beam is 1 mm, the displacement distance of OP is $-0.5 \text{ mm} \leq t \leq 0.5 \text{ mm}$. Fig. 5(a) shows the change of the sampling volume as a function of the tilted angle. For any tilted imaging systems except for special application, the tilted angle can range from 0° to 180° . However, we mainly use the tilted imaging systems for particle measurement. When a spherical droplet in the flow field is illuminated by the pulsed laser sheet, the reflected and first-order refracted light from the droplet are dominant in the wide-angle forward-scatter region around 30° – 80° [23]. Therefore, in this paper, we limited the tilted angle from 30° to 80° . For the Type-I system, as the tilted angle increases, the sampling volume increases, whereas for the Type-II system, the sampling volume decreases. For Fig. 5(b), considering these two types of tilted imaging systems, the sampling volume decreases with increasing focal length. However, the change is small, which is essentially constant. In Fig. 5(c), in terms of these two types of tilted imaging systems, the sampling volume decreases as the central magnification increases. When $\beta_o < 0.6$, with the increase of the central magnification, the sampling volume decreases quickly; when $\beta_o > 0.6$, with the increase of the central magnification, the sampling volume decreases slowly, which is substantially unchanged. In Fig. 5(d), for the Type-I system, with F -number increasing, the sampling volume increases first, and then remains constant, whereas for the Type-II system, the sampling volume remains constant as the F -number increases. The reason due to which the sampling volume remains constant is that the depth of field increases as the F -number increases. When the depth of field increases to a certain extent, the illumination beam is completely in the range of the depth of field. Therefore, when the thickness of the illumination beam is constant, the sampling volume remains unchanged from a certain F -number.

4. Experimental Results

To validate the measurement method of the sampling volume experimentally, the experimental setup was assembled. The experimental setup consisted of a CCD sensor, imaging lens, and

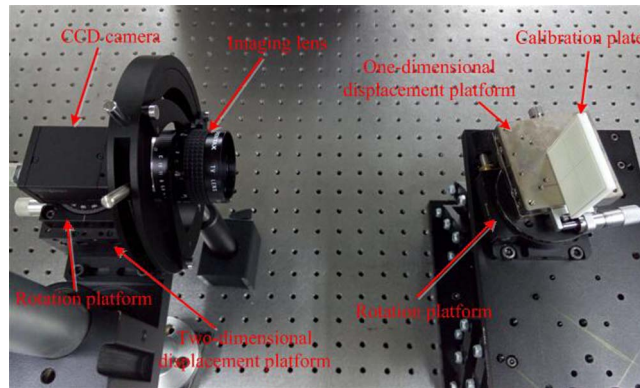


Fig. 6. Experimental setup.

ceramic grid calibration plate, as illustrated in Fig. 6. The CCD was a 14-bit digital CCD sensor from Point Grey (GRAS-14S5M-C) with $1384 \text{ pixels} \times 1036 \text{ pixels}$ and a pixel size of $6.45 \mu\text{m} \times 6.45 \mu\text{m}$. The imaging lens was a 50 mm f/1.4 PENTAX TV lens. The dimensions of the ceramic grid calibration plate were $50 \text{ mm} \times 50 \text{ mm}$ with a grid size of $2 \text{ mm} \times 2 \text{ mm}$ and linewidth of 0.05 mm . The measuring magnification was $\beta_o = 0.258$, along with $u_o = 243.8 \text{ mm}$, and $v_o = 62.9 \text{ mm}$. In the study, the calibration plate used for imaging was placed in the position of the OP, as shown in Fig. 1(a) and (b). The angle between the scribed line surface of the calibration plate and optical axis is θ . The geometric center of the scribed line surface of the calibration plate passes through the optical axis of the imaging lens. The geometric center of the CCD target surface also passes through the optical axis and is conjugate to the geometric center of the scribed line surface of the calibration plate. Two rotation platforms were used to control the tilted angles of OP and IP relative to the optical axis, respectively. A one-dimensional displacement platform placed under the calibration plate was employed to allow the calibration plate to move parallel at an interval $\Delta t = 0.1 \text{ mm}$, and the displacement distance is $-0.5 \text{ mm} \leq t \leq 0.5 \text{ mm}$. A 2-D displacement platform placed under the CCD sensor was used to adjust the focusing IP when $t = 0.0 \text{ mm}$. A sequence of calibration plate images can be acquired from the CCD sensor. Calibration plate images cut to a size of $600 \text{ pixels} \times 600 \text{ pixels}$ were processed by edge extraction, and the clear area of the OP that was the sampling area could be obtained. The integral of the sampling area for the displacement distance is the sampling volume at this tilted angle θ . Repeating the above steps for each tilted angle, we would obtain the relation between the sampling volume and the tilted angle to obtain the empirical calculating formula between the sampling volume and tilted angle.

Taking $\theta = 60^\circ$ as an example, for these two types of tilted imaging systems, the calibration plate images after edge extraction with a parameter $-0.4 \text{ mm} \leq t \leq 0.4 \text{ mm}$, $\Delta t = 0.2 \text{ mm}$ are presented in Fig. 7. Fig. 7(a)–(e) belong to the Type-I system, and Fig. 7(f)–(j) belong to the Type-II system. For the Type-I system, from $t = -0.4 \text{ mm}$ to $t = 0.4 \text{ mm}$, the calibration plate images move to the left collectively, and the sampling area primarily remains unchanged. For the Type-II system, from $t = -0.4 \text{ mm}$ to $t = 0.4 \text{ mm}$, the calibration plate images also move to the left collectively, and the sampling area gradually decreases, but with a slight change. Moreover, the magnification of the left and right side of a calibration plate image is not the same. For these two types of tilted imaging systems, the sampling area of the Type-II system is larger than that of the Type-I system.

Fig. 8 presents the calibration plate images after edge extraction at $t = 0.0 \text{ mm}$ and tilted angle $45^\circ \leq \theta \leq 75^\circ$, $\Delta\theta = 10^\circ$. Fig. 8(a)–(d) belong to the Type-I system, and Fig. 8(e)–(h) belong to the Type-II system. For the Type-I system, as the tilted angle increases, the sampling area also increases, whereas for the Type-II system, as the tilted angle increases, the sampling area decreases. For these two types of tilted imaging systems, the sampling area of the Type-II system is larger than that of the Type-I system.

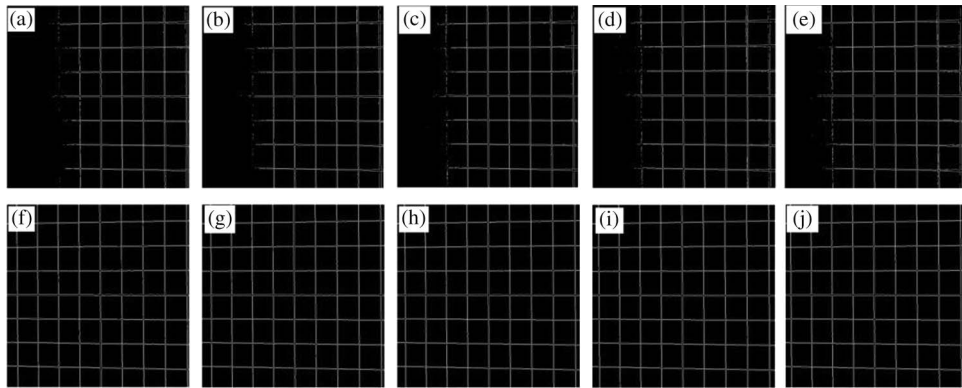


Fig. 7. Calibration plate images after edge extraction at $\theta = 60^\circ$. (a) $t = -0.4$ mm, (b) $t = -0.2$ mm, (c) $t = 0.0$ mm, (d) $t = 0.2$ mm, and (e) $t = 0.4$ mm belong to the Type-I system. (f) $t = -0.4$ mm, (g) $t = -0.2$ mm, (h) $t = 0.0$ mm, (i) $t = 0.2$ mm, and (j) $t = 0.4$ mm belong to the Type-II system.

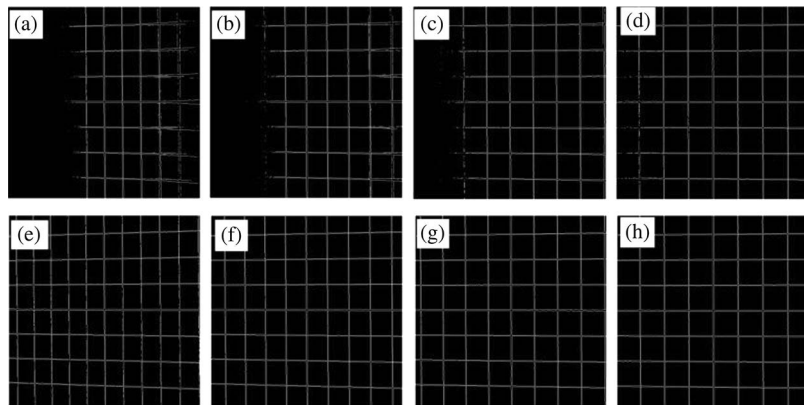


Fig. 8. Calibration plate images after edge extraction at $t = 0.0$ mm. (a) $\theta = 45^\circ$, (b) $\theta = 55^\circ$, (c) $\theta = 65^\circ$, and (d) $\theta = 75^\circ$ belong to the Type-I system. (e) $\theta = 45^\circ$, (f) $\theta = 55^\circ$, (g) $\theta = 65^\circ$, and (h) $\theta = 75^\circ$ belong to the Type-II system.

The sampling area could be obtained by extracting the clear part of the calibration plate images after edge extraction. The numerical values of the sampling area are presented in Table 1 for the Type-I system, and in Table 2 for the Type-II system.

The sampling volume is the integral of the sampling area for the displacement distance. The theoretical and experimental sampling volumes along with the change of the tilted angle with parameters $f = 50$ mm, $F = 1.4$, $\beta_o = 0.258$ are shown in Fig. 9. Fig. 9(a) presents the results for the Type-I system, and Fig. 9(b) presents the results for the Type-II system. The black line represents the theoretical values, and the red-star-shaped points represent the experimental values. The theoretical and experimental curves show the same trend. However, these two curves do not match perfectly. First, in theoretical analyzing the relationship between sampling volume and tilted angle, we have assumed these factors such as the central magnification of imaging system, focal length or F -number of imaging lens remain unchanged. However, in the actual experimental setup, these factors are impossible to remain unchanged, so they will have an effect on sampling volume. Second, in the process of acquiring an image, the incline of the object plane results in the uneven illumination of the image plane, thus affecting the contrast of calibration plate images. The uneven image will cause the image to exact difficult. Finally, the homogeneity of light source and the noise of CCD sensor also introduce errors. Therefore, the measurement errors inevitably occur, and it leads to the difference between theoretical predications and experimental results.

TABLE 1

Sampling area of the Type-I system

	$t = -0.4mm$	$t = -0.2mm$	$t = 0.0mm$	$t = 0.2mm$	$t = 0.4mm$
$\theta = 30^\circ$	47.25 mm ²	48.00 mm ²	48.75 mm ²	48.00 mm ²	48.00 mm ²
$\theta = 35^\circ$	52.17 mm ²	50.87 mm ²	51.52 mm ²	50.87 mm ²	47.61 mm ²
$\theta = 40^\circ$	61.18 mm ²	54.71 mm ²	51.76 mm ²	52.35 mm ²	62.35 mm ²
$\theta = 45^\circ$	62.63 mm ²	62.11 mm ²	62.11 mm ²	63.16 mm ²	61.05 mm ²
$\theta = 50^\circ$	68.36 mm ²	67.38 mm ²	66.89 mm ²	66.89 mm ²	67.87 mm ²
$\theta = 55^\circ$	74.77 mm ²	72.92 mm ²	72.92 mm ²	69.69 mm ²	75.23 mm ²
$\theta = 60^\circ$	76.29 mm ²	75.00 mm ²	72.86 mm ²	72.43 mm ²	78.00 mm ²
$\theta = 65^\circ$	97.92 mm ²	87.50 mm ²	87.08 mm ²	84.17 mm ²	89.58 mm ²
$\theta = 70^\circ$	108.00 mm ²	104.80 mm ²	107.20 mm ²	105.20 mm ²	106.40 mm ²
$\theta = 75^\circ$	144.55 mm ²	145.32 mm ²	139.48 mm ²	144.94 mm ²	142.60 mm ²
$\theta = 80^\circ$	198.99 mm ²	204.30 mm ²	208.86 mm ²	206.20 mm ²	179.62 mm ²

TABLE 2

Sampling area of the Type-II system

	$t = -0.4mm$	$t = -0.2mm$	$t = 0.0mm$	$t = 0.2mm$	$t = 0.4mm$
$\theta = 45^\circ$	318.86mm ²	317.66mm ²	315.45mm ²	315.11 mm ²	314.71 mm ²
$\theta = 50^\circ$	293.31 mm ²	292.77mm ²	292.39mm ²	292.08 mm ²	291.77 mm ²
$\theta = 55^\circ$	277.67 mm ²	277.09mm ²	276.58 mm ²	276.11 mm ²	275.56 mm ²
$\theta = 60^\circ$	259.91mm ²	259.39mm ²	258.95 mm ²	258.51 mm ²	257.98 mm ²
$\theta = 65^\circ$	249.71 mm ²	248.83 mm ²	248.18 mm ²	247.61 mm ²	247.16 mm ²
$\theta = 70^\circ$	240.98 mm ²	240.05 mm ²	239.10 mm ²	238.61 mm ²	238.20 mm ²
$\theta = 75^\circ$	236.49 mm ²	235.74 mm ²	235.09 mm ²	234.49 mm ²	233.75 mm ²
$\theta = 80^\circ$	230.25 mm ²	229.90 mm ²	229.53 mm ²	229.26 mm ²	228.98 mm ²

The blue line represents the fitted curve for the experimental values. The fitted curve for the Type-I system is $V = 8.987 \times 10^{-5}\theta^4 - 0.016\theta^3 + 1.103\theta^2 - 31.39\theta + 366.5$ with $R^2 = 0.9992$; the fitted curve for the Type-II system is $V = 0.0631\theta^2 - 10.31\theta + 651.6$ with $R^2 = 0.9978$. For the Type-I system, as the tilted angle increases, the sampling volume increases, whereas for the Type-II system, the sampling volume decreases. In addition, the sampling volume for the Type-II system is larger than that for the Type-I system.

5. Discussions

The sampling volume is correlated to the tilted angle, focal length, central magnification, and F -number. According to the simulation and experimental verification, for these two types of tilted imaging systems, the sampling volume decreases with increase in the focal length or central magnification. In addition, for the Type-I system, the sampling volume increases with increase in the tilted angle, and when the F -number increases, the sampling volume first increases, and then remains constant. For the Type-II system, the sampling volume decreases with increasing tilted angle, and the sampling volume remains constant as the F -number increases. Under the same condition, the sampling volume of the Type-II system is larger than that of the Type-I system. However, for the Type-II system, ellipses of confusion will be formed instead of circles of confusion on the CCD IP. Therefore, imaging may cause deformation. Moreover, smaller tilted angles result in more severe deformation.

In summary, to increase the sampling volume, the following steps should be used.

- For a Type-I system, select a larger tilted angle; for a Type-II system, select a smaller tilted angle under the premise to ensure a clear image.

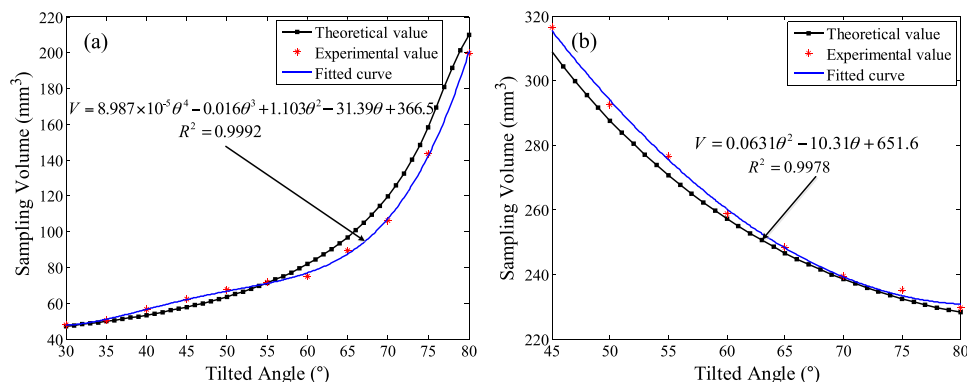


Fig. 9. Theoretical and experimental sampling volumes along with the change of the tilted angle with parameters $f = 50$ mm, $F = 1.4$, and $\beta_o = 0.258$. (a) Type-I system and (b) the Type-II system.

- b) For a Type-I or Type-II system, select a smaller central magnification.
- c) For a Type-I or Type-II system, select a larger F -number, which is associated with the focal length.
- d) For a Type-I or Type-II system, since the effect of the focal length is small, the selection of the focal length is associated with the F -number.

6. Conclusion

We presented a method to accurately calculate the sampling volume based on geometrical optics in two types of tilted imaging systems. We mainly studied the effect of the tilted angle on the sampling volume both theoretically and experimentally. The experimental results and theoretical predictions were in good agreement. For the Type-I system, as the tilted angle increases, the sampling volume increases, whereas for the Type-II system, the sampling volume decreases. In addition, the sampling volume of the Type-II system is larger than that of the Type-I system. Therefore, if a larger sampling volume is needed, the Type-II system should be selected. However, the magnification of different positions on the OP is not the same. This method has wider application in some fields using tilted imaging systems.

References

- [1] H. C. van de Hulst and R. T. Wang, "Glare points," *Appl. Opt.*, vol. 30, no. 33, pp. 4755–4763, Nov. 1991.
- [2] Y. Zama, M. Kawahashi, and H. Hirahara, "Simultaneous measurement of droplet size and three-components of velocity in spray," *Opt. Rev.*, vol. 11, no. 6, pp. 358–364, Sep. 2004.
- [3] C. F. Hess and D. L. Esperance, "Droplet imaging velocimeter and sizer: A two-dimensional technique to measure droplet size," *Exp. Fluids*, vol. 47, no. 1, pp. 171–182, Apr. 2009.
- [4] S. Dehaeck, J. van Beeck, and M. L. Riethmuller, "Extended glare point velocimetry and sizing for bubbly flows," *Exp. Fluids*, vol. 39, no. 2, pp. 407–419, Jun. 2005.
- [5] Y. Zama, M. Kawahashi, and H. Hirahara, "Simultaneous measurement method of size and 3D velocity components of droplets in a spray field illuminated with a thin laser-light sheet," *Meas. Sci. Technol.*, vol. 16, no. 10, pp. 1977–1986, Sep. 2005.
- [6] Y. Hardalupas, S. Sahu, A. M. K. P. Taylor, and K. Zargoulidis, "Simultaneous planar measurement of droplet velocity and size with gas phase velocities in a spray by combined ILIDS and PIV techniques," *Exp. Fluids*, vol. 49, no. 2, pp. 417–434, Jan. 2010.
- [7] C. Lacour, D. Durox, S. Ducruix, and M. Massot, "Interaction of a polydisperse spray with vortices," *Exp. Fluids*, vol. 51, no. 2, pp. 295–311, Feb. 2011.
- [8] J. F. Koretz, S. A. Strenk, L. M. Strenk, and J. L. Semmlow, "Scheimpflug and high-resolution magnetic resonance imaging of the anterior segment: A comparative study," *J. Opt. Soc. Amer. A, Opt. Image Sci.*, vol. 21, no. 3, pp. 346–354, Mar. 2004.
- [9] A. Wegener and H. L. Junga, "Photography of the anterior eye segment according to Scheimpflug's principle: Options and limitations—A review," *Clin. Exp. Ophthalmol.*, vol. 37, no. 1, pp. 144–154, Feb. 2009.

- [10] A. K. C. Lam, R. Chan, G. C. Woo, P. C. K. Pang, and R. Chiu, "Intra-observer and inter-observer repeatability of Anterior Eye Segment analysis system (EAS-1000) in anterior chamber configuration," *Ophthalmic Physiol. Opt.*, vol. 22, no. 6, pp. 552–559, Jun. 2002.
- [11] D. Kuerten *et al.*, "Central corneal thickness determination in corneal edema using ultrasound pachymetry, a Scheimpflug camera, and anterior segment OCT," *Graefes Arch. Clin. Exp. Ophthalmol.*, vol. 253, no. 7, pp. 1105–1109, Apr. 2015.
- [12] K. Kashiwagi *et al.*, "A newly developed peripheral anterior chamber depth analysis system: Principle, accuracy, and reproducibility," *Br. J. Ophthalmol.*, vol. 88, no. 8, pp. 1030–1035, Aug. 2004.
- [13] D. S. Grewal and S. P. S. Grewal, "Clinical applications of Scheimpflug imaging in cataract surgery," *Saudi J. Ophthalmol.*, vol. 26, no. 1, pp. 25–32, Jan. 2012.
- [14] B. R. Masters, "Three-dimensional microscopic tomographic imaging of the cataract in a human lens in vivo," *Opt. Exp.*, vol. 3, no. 9, pp. 332–338, Oct. 1998.
- [15] F. J. Shiou and W. Y. Cheng, "Development of an innovative multi-detector triangulation laser probe," in *Proc. IEEE Int. Conf. Mechatron.*, 2005, pp. 318–322.
- [16] W. Lei, B. Mei, G. Jun, and O. ChunSheng, "A novel double triangulation 3D camera design," in *Proc. IEEE Int. Conf. Inf. Acquisition*, 2006, pp. 877–882.
- [17] A. Miks, J. Novak, and P. Novak, "Analysis of imaging for laser triangulation sensors under Scheimpflug rule," *Opt. Exp.*, vol. 21, no. 15, pp. 18225–18235, Jul. 2013.
- [18] D. Callaud and L. David, "Stereoscopic particle image velocimetry measurements of the flow around a surface-mounted block," *Exp. Fluids*, vol. 36, no. 1, pp. 53–61, Jul. 2004.
- [19] A. K. Prasad and K. Jensen, "Scheimpflug stereocamera for particle image velocimetry in liquid flows," *Appl. Opt.*, vol. 34, no. 30, pp. 7092–7099, Oct. 1995.
- [20] B. He and F. Duan, "Full-field convection flow visualization in pendant droplets by tilt-angle imaging," *Appl. Phys. Lett.*, vol. 103, no. 5, Jul. 2013, Art. ID 053508.
- [21] Y. Yin, M. Wang, B. Z. Gao, X. Liu, and X. Peng, "Fringe projection 3D microscopy with the general imaging model," *Opt. Exp.*, vol. 23, no. 5, pp. 6846–6857, Mar. 2015.
- [22] W. Zheng, O. Hulthen, and S. Esmali, "Splice-loss estimation for an automated ribbon-fiber fusion splicer," *J. Lightw. Technol.*, vol. 17, no. 8, pp. 1366–1378, Aug. 1999.
- [23] T. Kawaguchi, Y. Akasaka, and M. Maeda, "Size measurements of droplets and bubbles by advanced interferometric laser imaging technique," *Meas. Sci. Technol.*, vol. 13, no. 3, pp. 308–316, Feb. 2002.